Available online at www.sciencedirect.com
ScienceDirect
Journal of the European Ceramic Society 30 (2010) 775–785
www.elsevier.com/locate/jeurceramsoc

Indentation analysis of elastic and plastic deformation of precursor-derived Si–C–N ceramics

Narayanan Janakiraman *, Fritz Aldinger

Max-Planck Institut für Metallforschung and Institut für Nichtmetallische Anorganische Materialien, Universität Stuttgart, Pulvermetallurgisches Laboratorium, Heisenbergstr. 3, D-70569 Stuttgart, Germany

Received 3 July 2009; accepted 8 September 2009
Available online 26 September 2009

Abstract

Elastic and plastic deformation behavior of precursor-derived Si–C–N ceramics at room temperature under contact loading was investigated using nano- and microindentation experiments. The observed behavior showed striking similarities to that of anomalous silicate glasses and amorphous carbon based films. The elastic deformation was controlled by the overall rigidity of the material microstructure, that evolved with the increase in the network connectivity due to progressive dehydrogenation in the amorphous materials, and the formation and organization of turbostratic graphite and nanocrystalline SiC in the phase-separated materials. The plastic deformation of the amorphous materials displayed anomalous densification inducing appreciable strain hardening, which reduced with progressive phase separation in the materials. The contrasting evolution of elastic and plastic deformation work quantities in amorphous and phase-separated materials indicate that the plastic deformation in former materials was volume deformation-controlled whereas that in the latter materials was interface deformation-controlled.

Keywords: B. Nanocomposites; C. Hardness; C. Mechanical properties; C. Plasticity; Densification

1. Introduction

Precursor-derived silicon based non-oxide ceramics are a new class of materials investigated for room- and high-temperature structural applications.[1] By virtue of their synthetic route, these materials are predominantly amorphous or nanocrystalline at the end of the precursor-to-ceramic transformation depending on the precursor chemistry and processing conditions,[2] and display brittle fracture behavior under remote loading, comparable to inorganic silicate glasses.[3–5] In a previous paper the fracture mechanical characterization of the title materials under remote loading was reported, where the crack-tip toughness (K_{I0}) was evaluated for a range of Si–C–N ceramics encompassing hydrogenated amorphous to nanocrystalline structures.[6] While the gross fracture behavior of amorphous ceramics is evidently brittle at the macro- and micro-scale regimes, the possibility of inelastic permanent deformation at crack tips preceding fracture in the nano-scale regime is currently under intense study.[7,8] This possibility was investigated with respect to amorphous Si–C–N ceramics and was found that the fracture proceeds by brittle cleavage even at length scales of the order of few tens of nanometers at the employed crack velocities.[9] In contrast to the deformation behavior under remote loading, permanent plastic deformation in inorganic glasses and amorphous ceramics under contact loading, e.g., by sharp indenters is well documented, and is known to arise due to the tri-axial compressive stress state in the contact zone.[10,11] As precursor-derived ceramics (PDC) are envisaged for tribological applications[12] and in MEM device components[13] where contact loading is prevalent, understanding of the elastic and plastic deformation behavior of these materials under contact loading is important.

Previous studies have revealed that the deformation behavior of PDC under indentation is also comparable to that of silicate network glasses.[14,15] Specifically, the permanent deformation in amorphous Si–C–O and Si–C–N PDC under the indenter has been identified to display anomalous behavior, occurring predominantly by the non-volume conserving densification rather than the volume conserving shear flow, commensurate with the

* Corresponding author. Present address: Institut für Nichtmetallische Werkstoffe, Technische Universität Clausthal, Zehntnerstr. 2a, 38678 Clausthal-Zellerfeld, Germany. Tel.: +49 5323 72 3537; fax: +49 5323 72 3710.
E-mail address: nja@tu-clausthal.de (N. Janakiraman).

0955-2219/$ – see front matter © 2009 Elsevier Ltd. All rights reserved.
doi:10.1016/j.jeurceramsoc.2009.09.006

estimated low values of (elastic modulus normalized) residual stresses.[14,15] Evaluation of the nanoindentation hardness and elastic modulus of an amorphous Si–C–N ceramic was reported by Galusek et al.,[16] although the results were influenced by porosity in the samples. Apart from this work and a few microhardness evaluations of Si–C,[5] Si–O–C[14,17] and Si–C–N[18] PDC, no systematic quantitative investigations on the indentation deformation of PDC have been carried out until now, partly due to the unavailability of fully dense homogeneous test specimens. Additionally, it is obvious that the relative extent of densification and shear flow during plastic deformation cannot be distinguished from the measured values of indentation hardness. This distinction can be important in controlling the evolution of material resistance to deformation beyond the elastic limit.

In this paper, a detailed investigation of the elastic and plastic deformation in precursor-derived Si–C–N ceramics by spherical and Berkovich indentation is presented, using depth-sensing nanoindentation measurements. Adopting the well established Oliver–Pharr method,[19] the evolution of indentation hardness and elastic modulus are evaluated for a series of Si–C–N PDC varying in material structures, from partly hydrogenated amorphous to phase-separated nanocrystalline states. From the analysis of reversible and irreversible energies evaluated from the indentation load–unload cycle, contributions from the elastic and plastic deformation during indentation are discussed in correlation with hardness and elastic modulus. The effect of applied load on hardness is examined from the measurement of Meyer hardness using Vickers microindentation at loads ranging from 0.245 to 49.05 N. The pile-up and sink-in behavior is probed by atomic force microscopy (AFM) imaging of residual impressions from Vickers indentation.

2. Experimental procedure

2.1. Materials

Fully dense monolithic Si–C–N ceramics were prepared from the liquid poly(ureamethylvinyl)silazane precursor through a casting route. Details of the processing as well as the structural and phase characterization of the resultant materials are described elsewhere.[20] In brief, the process involves the thermal cross-linking of the liquid precursor, cast and sealed in PTFE molds, followed by pyrolysis of the obtained pore-free transparent green bodies in flowing argon atmosphere, up to various final pyrolysis temperatures between 800 and 1300 °C. By this way, a range of material structures of the final ceramic products were realized, varying from partly hydrogenated amorphous to nanocrystalline microstructures. The materials are denoted here, code-named according to their thermal treatment, *viz.*, SiCN-080001, SiCN-090001, SiCN-100001, SiCN-110001, SiCN-120012 and SiCN-130012, the first four digits denoting the temperature and the last two digits, the hold time of the final pyrolysis or annealing treatment in hours. The materials SiCN-080001 through SiCN-110001 are electron-amorphous, whereas the remaining two possess phase-separated microstructures. The resultant ceramic bodies were subsequently ground and polished in the form of thin (200–400 μm) rectangular plates with dimensions 8 mm × 4 mm, with the final surface finishing performed with a 0.25 μm diamond suspension.

2.2. Indentation

Nanoindentation experiments were performed using a *Nano Indenter® XP* nanoindentation system (MTS Nano Instruments, Oak Ridge, TN, USA), located in a temperature and atmosphere controlled laboratory. Two sets of nanoindentation measurements were made using a Berkovich indenter. In the first set, *P–h* curves were recorded with five different maximum loads (P_{max}) of 25, 50, 100, 200 and 500 mN, using the following schedule: 30 s loading to P_{max}; 10 s hold at P_{max}; and 30 s to full unload. In the second set, *P–h* curves were recorded in the continuous stiffness measurement (CSM) mode under the following parameters: load cycle depth limit target ≈1500 to 1950 nm (leading to $P_{max} \approx 450$ to 490 mN); strain rate target: 0.05 s^{-1}; superimposed harmonic amplitude limit: 2 nm; harmonic frequency: 45 Hz; 10 s hold at P_{max}; 20 s to 90% unload; and 50 s hold at $0.1P_{max}$ for drift correction followed by full unload. For both the above measurements, ten indentations were made for each sample-load combination for statistical evaluation. Nanoindentation *P–h* curves using a spherical tipped indenter (tip radius (R_{sph}) = 150 μm) were recorded with P_{max} = 500 mN using the following schedule: 60 s loading to P_{max}; 10 s hold at P_{max}; and 60 s to full unload. A minimum of thirty measurements were made for each material, and the data that showed significant deviation from the spherical contact exponent of 1.5, arising from imperfect initial contact were discarded. Prior to actual measurements, the nanoindentation system was calibrated for frame compliance and tip shape imperfection using a fused silica standard specimen.

Vickers microindentation was performed using a *Micromet 1* microhardness tester (Buehler Ltd., Lake Bluff, IL, USA) for indentation loads 0.245, 0.490, 0.981, 1.962, 4.905 and 9.81 N, and using a *Zwick* indentation instrument (Zwick & Co. KG, Einswingen, Germany) for loads 19.62 and 49.05 N with a dwell time of 15 s at maximum load. Four to six indentations were made at each load. AFM topographic imaging of the residual Vickers impressions was carried out in taping mode using a *Multimode Nanoscope IIIa* AFM (Digital Instruments, Veeco Metrology Group, Santa Barbara) and standard Si probe tips. The images were recorded in height and amplitude contrasts simultaneously. The former contrast served to dimensionally quantify the topography via section analysis, while the latter enabled to resolve the finer variations or features in topography.

3. Results

3.1. Analysis of loading curves and tip imperfection – Berkovich indentation

The representative *P–h* curves recorded from Berkovich nanoindentation of specimens SiCN-080001 through SiCN-130012 are shown in Fig. 1. For visual clarity, only the data from the 500 mN load is included. In order to examine the

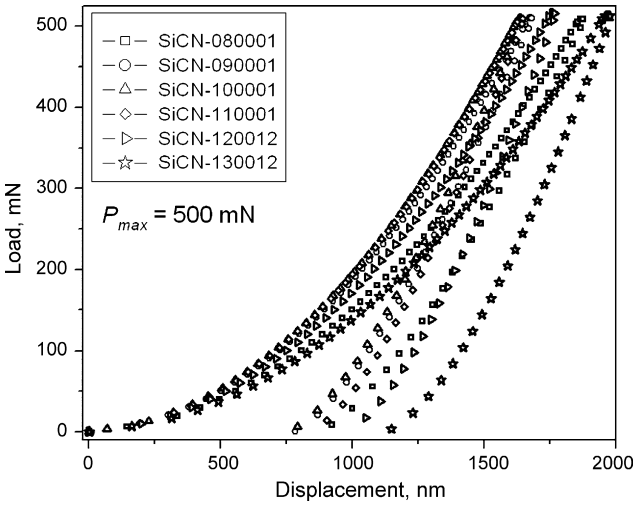

Fig. 1. Representative *P–h* curves from Berkovich nanoindentation of Si–C–N ceramics with $P_{max} = 500$ mN.

square dependence of displacement (h) to the load (P) in the loading curve as expected from ideal self-similar indenters,[21] least square fitting of the loading curve data from loads 25 through 500 mN was performed according to the general power expression:

$$P = Ah^{x_f}. \tag{1}$$

The loading curve exponent $x_l = x_f$ from the curve fits varied from 1.81 to 1.97 for loading curves from $P_{max} = 25$ mN through 500 mN, while showing negligible dependence to the material being indented. Accordingly, the deviation from the square dependence can be ascribed to the indenter tip imperfection. Assuming that the actual tip has worn to a spherical shape, the tip radius R_{Berk} was estimated following the procedure described by Cheng and Cheng[22] by least square fitting of the measured loading curves according to the quadratic polynomial expression

$$P = c_0h^2 + c_1h + c_2, \tag{2}$$

from which R_{Berk} was estimated as

$$R_{Berk} = \frac{c_1}{2c_0((1/\sin\psi) - 1)}, \tag{3}$$

where $\psi = 70.3°$ for Berkovich indenter. The derived values showed wide scatter with $R_{Berk} \approx 360 \pm 160$ nm. As the loading curves from 500 mN loading are the least influenced with respect to the tip imperfection, the evolution of material parameters across different materials will be discussed in the following, mainly based on the analysis of these *P–h* curves, except where load dependence of the material behavior is observed.

3.2. Oliver–Pharr analysis – Berkovich indentation

Towards evaluating elastic modulus and hardness of the materials, the Oliver–Pharr analysis[19] was applied, along with the recent refinements presented by the same authors in Ref. 23. Accordingly, the unloading curves were least square fitted to the expression:

$$P = B(h - h_{res})^{x_{ul}}, \tag{4}$$

where h_{res} is the residual depth at full unload, and x_{ul} is the unloading curve exponent. The derived values of x_{ul} increased from 1.39 to 1.49 in materials SiCN-080001 through SiCN-130012 respectively, while a smaller increase was also observed with increasing maximum load, P_{max}. The unloading slope (S) was evaluated from the derivative of Eq. (4) at P_{max}. The true contact depth (h_c) was evaluated from the relation

$$h_c = h_{\max} - \chi\left(\frac{P_{\max}}{S}\right), \tag{5}$$

where the geometric parameter χ was explicitly evaluated from Eq. (17) in Ref. 23 using the value of x_{ul} for each unloading curve. The value of χ showed only a marginal variation in the range $0.76 \le \chi \le 0.75$. The true contact area (A_c) was evaluated taking into account the tip imperfection via the use of an area function calibrated using fused silica standard. Further, the elastic modulus (E) and hardness (H) were evaluated from the relations:

$$E_r = \frac{1}{\beta}\frac{\sqrt{\pi}}{2}\frac{S}{\sqrt{A_c}}; \tag{6}$$

$$\frac{1}{E_r} = \frac{1-\nu^2}{E} + \frac{1-\nu_i^2}{E_i}; \tag{7}$$

and

$$H = \frac{P_{\max}}{A_c}. \tag{8}$$

A value of $\beta = 1.05$ was used in Eq. (6).[23] The values $E_i = 1141$ GPa and $\nu_i = 0.07$ were used as the elastic modulus and poisons ratio of the diamond indenter. The poisons ratios of the investigated Si–C–N materials were 0.245, 0.24, 0.22, 0.21, 0.22 and 0.23 for materials SiCN-080001 through SiCN-130012, respectively, obtained from the resonance frequency testing using circular disk specimens.[20] The evolution of elastic modulus and hardness in materials SiCN-080001 through SiCN-130012 evaluated from the unloading curve analysis as above is presented in Fig. 2(a) and (b), respectively. The elastic modulus increased in amorphous materials SiCN-080001 through SiCN-110001 from 95 through 140 GPa, and decreased in the phase-separated materials SiCN-120012 and SiCN-130012 to 129 GPa and 105 GPa, respectively. Elastic moduli of these materials have been determined independently by resonance frequency testing (82, 106, 117, 127, 140, and 117 GPa for materials SiCN-080001 through SiCN-130012, respectively)[20] and represent the mean behavior from the whole specimen bulk. Compared to these values, the elastic moduli from the unloading curve analysis were higher by 10 to 15% for the amorphous materials and by 8 to 10% lower for the phase-separated materials. The nanoindentation hardness increased from 12.4 to 15.7 GPa in materials SiCN-080001 through SiCN-100001 and decreased from 14.5 to 9.3 GPa in materials SiCN-110001 through SiCN-130012. On the other hand, the variations of E and H with increasing maximum indentation loads from 50 through 500 mN

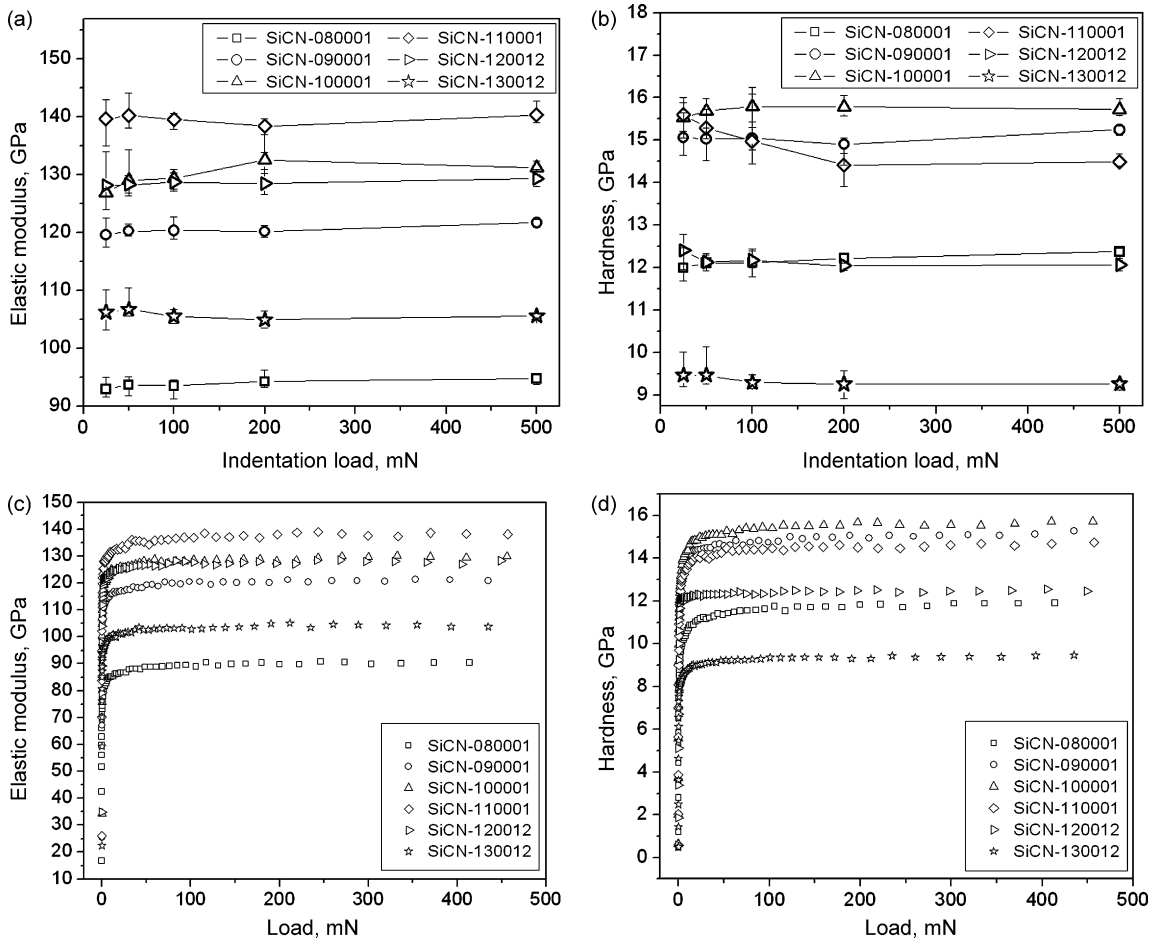

Fig. 2. Elastic modulus (a) and hardness (b) of Si–C–N ceramics determined from Oliver–Pharr analysis of Berkovich nanoindentation data obtained at $25\,\text{mN} \leq P_{max} \leq 500\,\text{mN}$. (c) and (d) show the evolution of elastic modulus and hardness determined from CSM analysis. Lines connecting data points serve as guide to the eye.

were comparatively small. The above results are in excellent agreement with those from the CSM analysis, Fig. 2(c) and (d), where the evolution of respectively E and H, with progressively increasing load is plotted.

3.3. Oliver–Pharr analysis – spherical indentation

Plastic deformation invariably accompanies elastic deformation during sharp indentation and has been recently supposed to affect elastic modulus measurements in PDC.[24] In order to verify this possibility on the elastic moduli determined as above, the moduli of three materials, SiCN-080001, SiCN-110001 and SiCN-130012 that cover the entire range of the investigated Si–C–N material structures, were independently evaluated by spherical indentation within the elastic contact regime. The representative P–h curves recorded from these measurements with $P_{max} = 500\,\text{mN}$ are presented in Fig. 3. The respective loading and unloading curves overlap with each other for all the three materials, indicating that the deformation was completely elastic during the experiments. Least square fitting of the unloading curves according to Eq. (1) also showed that the unloading curve exponents $x_{ul} = x$ varied in the range $1.49 \leq x_{ul} \leq 1.53$, closely comparing with the theoretical value of 1.5 expected for elastic spherical contact loading. The elastic moduli of the materials were evaluated by applying the Oliver–Pharr method of unloading curve analysis for spherical indentation.[25] The contact depth h_c was evaluated from Eq. (5) with $\chi = 0.75$ verified as

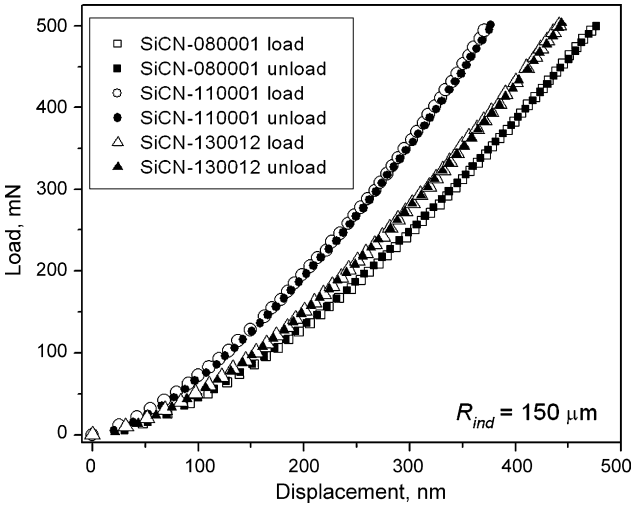

Fig. 3. Representative P–h curves from spherical nanoindentation of Si–C–N ceramics with $P_{max} = 500\,\text{mN}$.

described earlier. That the contact loading was elastic was also verified from the ratio h_c/h_{max} yielding a value of 0.507 ± 0.02, comparing well with the theoretically expected value of 0.5.[25] The contact radius (a_c), contact area (A_c) and the mean contact pressure (p_m) at maximum load P_{max} were evaluated from the relations:

$$a = \sqrt{2h_c R - h_c^2}; \tag{9}$$

$$A_c = \pi a_c^2; \tag{10}$$

and

$$p_m = \frac{P_{\max}}{\pi a_c^2}. \tag{11}$$

E_r and E were evaluated respectively from Eqs. (6) and (7) with $\beta = 1$ in accordance with spherical indentation.[23] The values of E were found to be 96.8 ± 1.4 GPa, 141 ± 4.7 GPa and 113 ± 4.2 GPa for materials SiCN-080001, SiCN-110001 and SiCN-130012 respectively, in good agreement with those derived from the Berkovich indentation analysis. This shows that the elastic moduli determined by the latter analysis were not drastically influenced by plastic deformation. Specifically, the measurements were unaffected by errors due to pile-up or sink-in effects. However, as mentioned in the previous section, small variations were indeed observed at increasing applied loads for Berkovich indentation. This load effect will be further described in Section 3.5. The mean contact pressures (p_m) at P_{max} were 2.18 ± 0.07 GPa, 2.77 ± 0.17 GPa and 2.41 ± 0.18 GPa in the respective materials. Evidently, these values are far less than the contact pressures (hardness) realized in the Berkovich indentation experiments.

3.4. Analysis of the load–unload cycle

While the elastic modulus and nanoindentation hardness evaluated as above quantify the overall variations in the elastic and plastic deformation in the materials during contact loading, they do not completely describe the nature of the deformation process. Previous studies have shown that more insight into such processes is gained by the analysis of the load–unload cycle.[21,23,26] The widely studied parameters in this approach are the residual depth of penetration (h_{res}), total work of contact deformation (W_{tot}), work from elastic recovery (W_{el}) and the work of inelastic deformation (W_{pl}). The numerical values of the quantities W_{tot}, W_{el} and W_{pl} can be directly obtained from the load–unload P–h cycle, as the area under the loading curve, under the unloading curve and the area enclosed by the two curves, respectively. A schematic of the nanoindentation load–unload cycle illustrating the above parameters is shown in Fig. 4. For efficient analysis the depth quantities are usually normalized with the depth at maximum load h_{max} and the work quantities are normalized with the total work W_{tot}, leading to the characteristic ratios, e.g., h_{res}/h_{max}, W_{pl}/W_{tot}, W_{el}/W_{tot}, etc. The residual depth ratio h_{res}/h_{max} and plastic work ratio W_{pl}/W_{tot} characterize the extent of plastic deformation during contact loading and thus were examined with respect to the deformation behavior of the present Si–C–N materials.

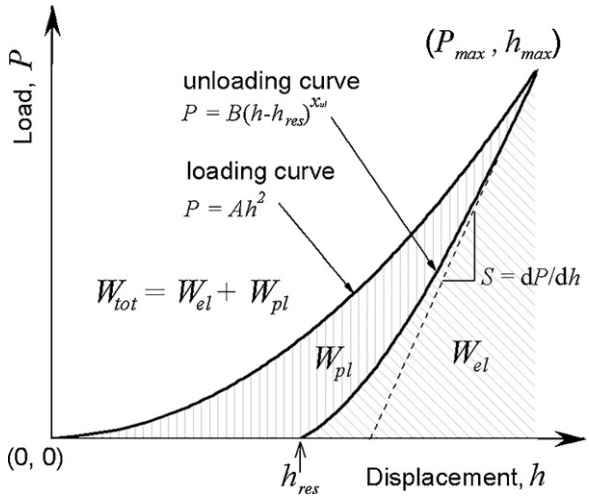

Fig. 4. Schematic of the nanoindentation loading–unloading cycle illustrating key experimental parameters.

The evolutions of the ratios h_{res}/h_{max} and W_{pl}/W_{tot} in materials SiCN-080001 through SiCN-130012 are presented in Fig. 5(a) and (b), respectively. The residual depth ratio decreased slightly from 0.46 to 0.44 in materials SiCN-080001 through SiCN-100001 and increased from 0.50 to 0.56 in materials SiCN-110001 through SiCN-130012. This variation correlates well with the evolution of hardness in the corresponding materials. In comparison, the plastic work ratio increased from 0.41 to 0.49 in materials SiCN-110001 through SiCN-130012, but remained nearly constant at 0.34 in materials SiCN-080001 through SiCN-100001. The correlation between the residual depth ratio and plastic work ratio is presented in Fig. 5(c). The increase in the residual depth ratio and plastic work ratio in materials SiCN-110001 through SiCN-130012 displayed a linear correlation, indicating the progressively increasing extent of plastic deformation in these materials. The slope of this linear correlation was identical with that reported by Cheng and Cheng[21] (dotted line in Fig. 5(c)), expressed by the relation

$$\frac{W_{pl}}{W_{tot}} = (1+\gamma)\frac{h_{res}}{h_{\max}} - \gamma \tag{12}$$

for $h_{res}/h_{max} > 0.4$ and $\gamma = 0.27$. However, the overall residual depth ratios were shifted towards lower values by 0.02–0.04, the higher shift corresponding to lower indentation load, or in other words, lower probing depth (further described in the next section). In contrast, the materials SiCN-090001 and SiCN-080001 did not follow the above linear correlation, due to the invariance in plastic work ratio even at increasing residual depth ratios. Relative to the linear trend observed for the other materials, this deviation can be translated into enhanced elastic recovery in these materials. For comparison, the correlation data for fused silica evaluated from the P–h curve reported in Ref. 23 is included in Fig. 5(c), which showed a larger residual depth ratio, while the plastic work ratio was nearly equal to that of materials SiCN-080001 through SiCN-100001. This means that the elastic recovery in fused silica was even higher than in SiCN-080001. Interpretation of these variations is further facilitated by comparing with the corresponding vari-

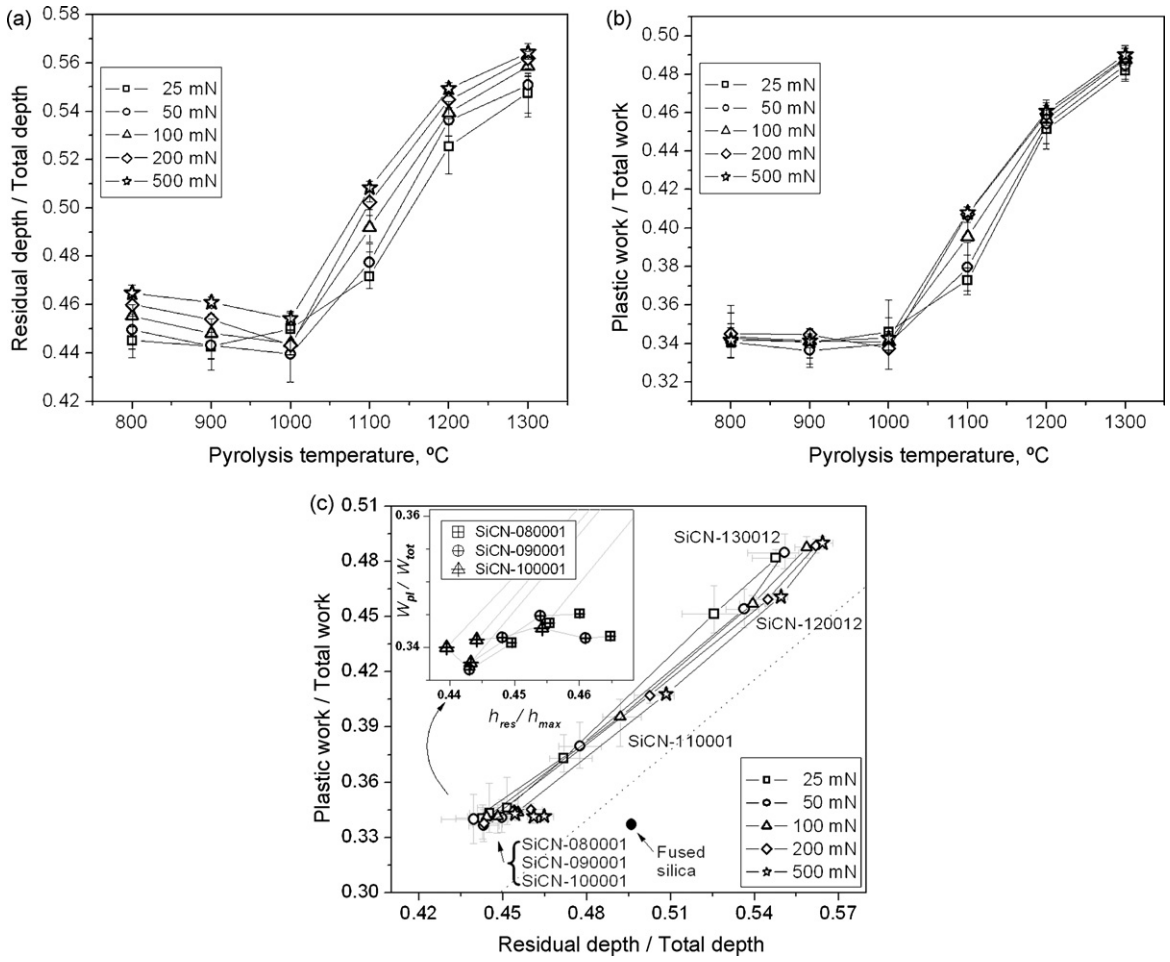

Fig. 5. Evolution of the ratios h_{res}/h_{max} (a), W_{pl}/W_{tot} (b) and the correlation between the ratios h_{res}/h_{max} and W_{pl}/W_{tot} (c) evaluated from the load–unload cycle data from Berkovich nanoindentation. The dotted line in (c) is the linear correlation reported in Ref. 21. The data point of fused silica (full circle) is derived from the *P–h* curve reported in Ref. 23. The region covering the amorphous ceramics SiCN-080001 through SiCN-100001 is magnified in the inset for clarity.

ations in the elastic modulus and hardness. For this purpose the ratio between the hardness and plane–strain elastic modulus, *viz.*, H/E^* (where $E^* = E/(1-\nu^2)$) is useful.[21] The evolution of H/E^* in materials SiCN-080001 through SiCN-130012 is presented in Fig. 6(a). The H/E^* ratio decreased from 0.123 to 0.114 in materials SiCN-080001 through SiCN-100001 and further more rapidly from 0.099 to 0.083 in materials SiCN-110001 through SiCN-130012. The decrease of H/E^* in the former materials was dominated by the increase in E^* whereas in the latter materials it was controlled by the reduction in hardness. The correlation between the plastic work ratio and H/E^* is presented in Fig. 6(b). For materials SiCN-110001 through SiCN-130012, a linear correlation was observed, reinforcing the result in Fig. 5(c). The slope of this linear correlation was also in agreement with the finite element analysis (FEA) simulated correlation data in Ref. 21, while the overall data were relatively shifted towards lower H/E^* values. Again, the materials SiCN-090001 and SiCN-080001 showed deviation from this linear correlation, with progressively higher H/E^* ratios (due to the higher elastic recovery, leading to lower contact stiffness S and thereby, lower E^*) at constant plastic work ratio equal to that of SiCN-100001. A still higher H/E^* ratio at comparable plastic work ratio was observed in fused silica (shown as full circle in Fig. 6(b)) confirming its further enhanced elastic recovery. For completion, the absolute and normalized indentation work of elastic, plastic and total deformations, derived from the *P–h* curves at 500 mN loading are presented in Fig. 7. Normalization was performed with the work quantities of SiCN-100001 material. The work quantities of fused silica were derived from the *P–h* curve from Ref. 23, duly accounting for the difference in the applied maximum loads. The normalized elastic and plastic work data for amorphous materials SiCN-100001 through SiCN-080001 and fused silica nearly overlapped on a single curve, showing that the progressively increasing plastic deformation is matched by a concomitant equi-proportional increase in the elastic recovery, manifested in the invariance of plastic work ratio. The same behavior was observed for indentation at lower loads down to 25 mN. These results are suggestive of a common deformation mechanism operative in these materials. As fused silica is known to plastically deform primarily by densification,[27] it can be reasoned that the invariance of plastic work ratio in materials SiCN-080001 through SiCN-100001 arised due to the prevalence of the same mechanism in these materials. On the other hand, the elastic and plastic work data for materials SiCN-110001 through SiCN-130012 predominantly showed an anti-correlation, indicating that their

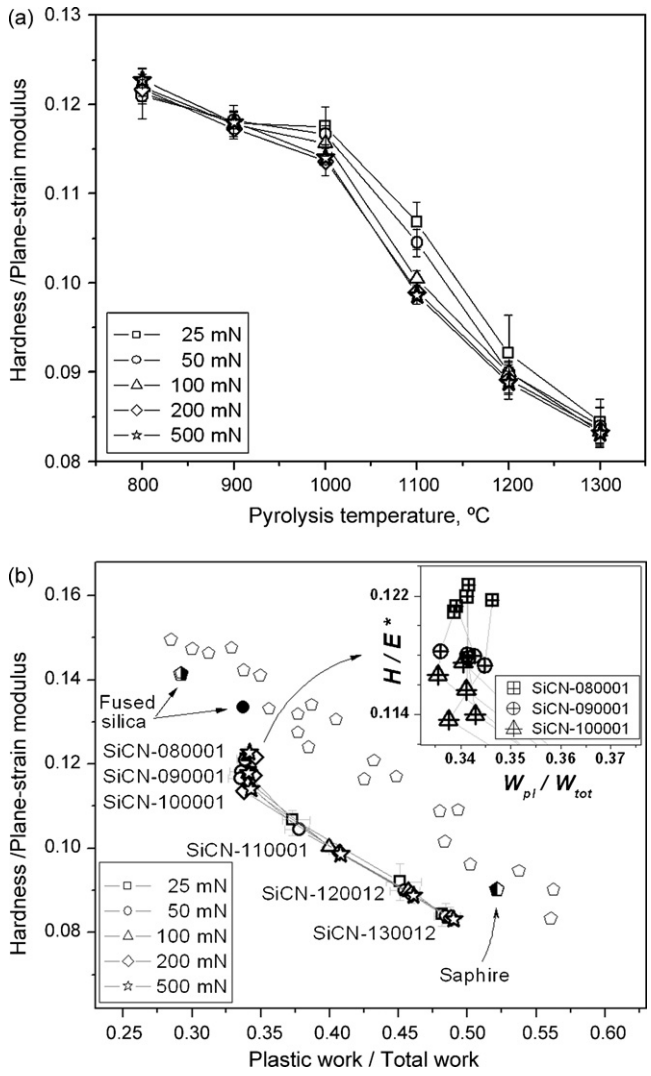

Fig. 6. Evolution of the ratios H/E^* (a) and the correlation between the ratios W_{pl}/W_{tot} and H/E^* (b) evaluated from the load–unload cycle data from Berkovich nanoindentation. The correlation data of the same ratios reported in Ref. 21 (half-filled pentagons: experimental data from fused silica and sapphire; open pentagons: FEA simulated data) are also included for comparison. The second data point (full circle) of fused silica is derived from the P–h curve reported in Ref. 23. The region covering the amorphous ceramics SiCN-080001 through SiCN-100001 is magnified in the inset for clarity.

deformation mechanism is different from that in the former materials.

3.5. Load/size effect on hardness

A significant influence of the applied load was noted in all the measured elastic and plastic deformation parameters. The following observations were made, pertaining to the increase of load from 25 to 500 mN: (i) residual depth ratio increased uniformly in all the materials; (ii) plastic work ratio remained practically constant in materials SiCN-080001 through SiCN-100001, but increased in materials SiCN-110001 through SiCN-1300012, the increase in SiCN-110001 being appreciable; (iii) hardness increased in materials SiCN-080001 through SiCN-100001, but decreased in materials SiCN-110001 through SiCN-1300012, with a highest decrement in SiCN-110001 correlating with the increase in plastic work ratio; (iv) elastic modulus increased in samples SiCN-080001 through SiCN-120012, with a highest increment in SiCN-100001. These variations are relatively small compared to the inter-material variations describing material properties. However, they merit consideration from the view point of indentation size effect (ISE). From the uniform increase in the residual depth ratios, it is clear that the increase in load enhances plastic deformation in all the materials, commonly observed as the manifestation of ISE. Even so, the evolution of hardness proceeded in different directions in the amorphous (SiCN-080001 through SiCN-100001) and phase-separated materials, as observed above. It is to be noted that if the observations (i)–(iv) were to be due to the tip imperfection, it should affect the behavior of all the materials in the same direction. The invariance of plastic work ratio juxtaposed with the increase in residual depth ratio at increasing loads in the former materials revealed that the increased plastic deformation was matched by increased elastic recovery as described in the previous section. Identification of this behavior with the densification type of plastic deformation further suggests that the increase in hardness in these materials is related to densification of the material under the indenter. The decrease of hardness in the latter materials by corollary can be related to either a change or emergence of an additional plastic deformation mechanism, also indicated by the increase in plastic work ratios.

Traditionally, ISE is studied in the load range extending from nano- to microindentation regimes. To further examine the deformation behavior in the latter regime, microindentation experiments were performed using Vickers indentation at loads ranging from 0.245 to 49.05 N, and the Meyer hardness (H_M) of the materials SiCN-080001 through SiCN-130012 was evaluated according to the relation

$$H_M = \frac{P}{2d^2}, \tag{13}$$

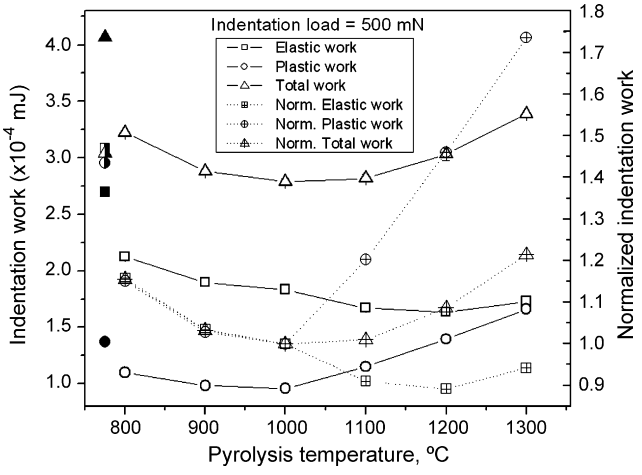

Fig. 7. The evolution of elastic, plastic and total work of indentation in amorphous and phase-separated Si–C–N ceramics; crossed symbols are indentation work normalized with those from SiCN-100001. Filled and half-filled symbols show respectively absolute and normalized work data from fused silica.

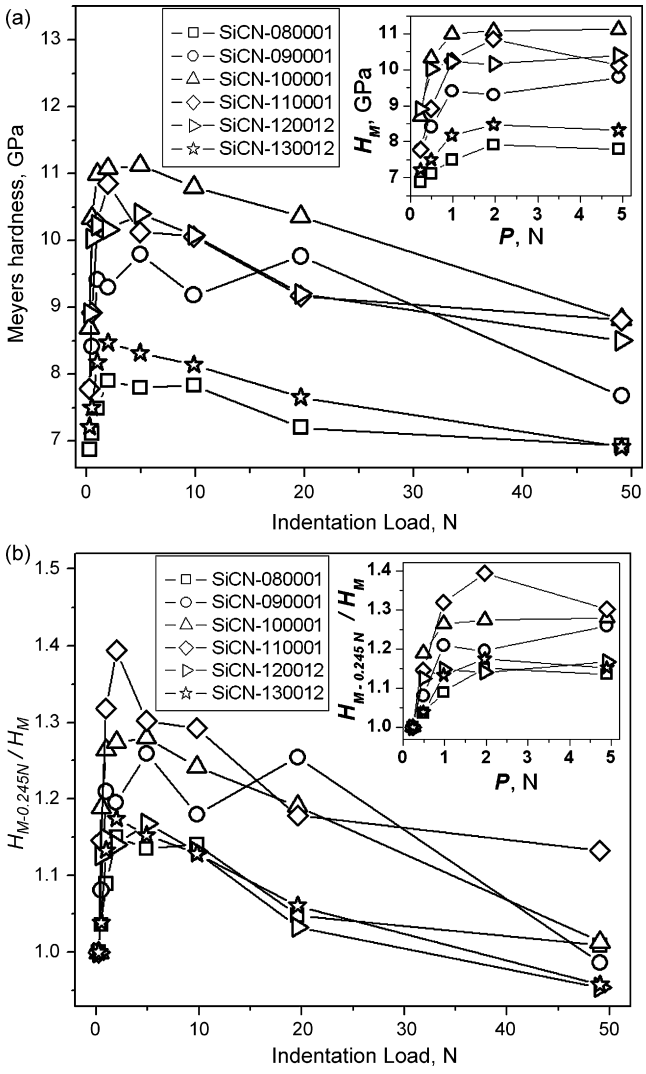

Fig. 8. (a) Evolution of Meyers hardness in Si–C–N ceramics, determined from Vickers microindentation at loads ranging from 0.245 N to 49.05 N; (b) Meyers hardness data in (a) normalized by the values measured at the lowest load of 0.245 N. The low load region is highlighted in the insets for visual clarity.

where P is the indentation load and d is the half of the indentation impression diagonal. The results are presented in Fig. 8(a). The Meyer hardness values were significantly lower than the nanoindentation hardness values as has been usually observed for various materials in the literature.[28] On the other hand, a continuous increase in H_M was observed for all the materials with increasing load in the range $0.245 \leq P \leq 4.905$ N (inset in Fig. 8(a)), followed by a continuous drop at further increasing load up to 49.05 N. For effective comparison of the variations across different materials, the H_M values at each load were normalized with the value measured at the lowest load, *viz.*, 0.245 N. The normalized data are plotted in Fig. 8(b). From these plots it was seen that hardness increased by a factor of 1.15, 1.19, 1.27, 1.39, 1.14 and 1.17 in the load range $0.245 \leq P \leq 2$ N for materials SiCN-080001 through SiCN-130012, respectively. (This increase was nearly nullified at still higher loads, except for SiCN-110001.) Comparing the effect of load on hardness in the nano- and microindentation experiments, two prominent differences were noted: (i) the factor of increase was appreciably higher in the latter experiments, even in the load range comparable in both nano- and microindentation, *viz.*, between 250 and 500 mN (inset in Fig. 8(b)); (ii) increase in microindentation hardness was also observed in materials SiCN-110001 through SiCN-130012, in contrast to nanoindentation experiments where a decrease in hardness was registered. However, it should also be noted that the two experiments differ with respect to the load regimes as well as the employed loading rates. The evolution of material resistance to plastic deformation depends on both of the above factors, *viz.*, load (transformed into indentation size and strain) via strain hardening and loading rate (transformed into strain rate) via strain rate sensitivity.

3.6. Pile-up and sink-in behavior

In order to examine the manifestation of plastic deformation and the strain hardening characteristics on the transport of the deformed material around the indenter, AFM topographic imaging of the residual indentation impressions were carried out. The residual impressions from Vickers indentation at $P = 4.905$ N were chosen for this purpose as they have the potential of exhibiting the maximum effect due to the high loads employed. Note that the increase in Meyer hardness reached saturation at this load (see Fig. 8). The recorded images of indents from materials SiCN-080001, SiCN-110001, SiCN-120012 and SiCN-130012 are depicted in Fig. 9. The images showed pile-up of deformed material around the indent impressions in the amorphous materials SiCN-080001 and SiCN-110001, with the magnitude being appreciably higher in the former as evident from the section analysis. Except at the inner core, the impression surfaces were nearly smooth, devoid of any shear faults. (The smaller irregular features were due to artifacts replicating the surface imperfections on the indenter surface.) Fine symmetrical steps resembling shear faults were observed at the impression core for both materials, which were well defined in SiCN-080001 than in SiCN-110001. While no pile-up at the impression edge was observed in the phase-separated materials SiCN-120012 and SiCN-130012, irregular shaped shear faults appeared at the impression surface, their number density increasing from SiCN-120012 to SiCN-130012. From the height contrast images, it is evident that the edge curvature of the impression cavities progressively decreased (leading to the transition from a pin-cushion shape towards a regular square) in materials SiCN-080001 through SiCN-130012. This shape change is irrespective of piling up but indicates that the elastic recovery in the materials decreased in the same order. This is also in agreement with the progressive increase in the ratio h_{res}/h_{max} from the nanoindentation measurements of these materials. On the other hand, the appearance of pile-up in materials SiCN-080001 and SiCN-110001 is suggestive of perfect-plastic deformation behavior, at least at the moment when the pile-ups were formed. The absence of pile-up for materials SiCN-120012 and SiCN-130012 implies either a change in yielding and strain hardening character in these materials, or a change in the friction character of the indenter-impression interface.

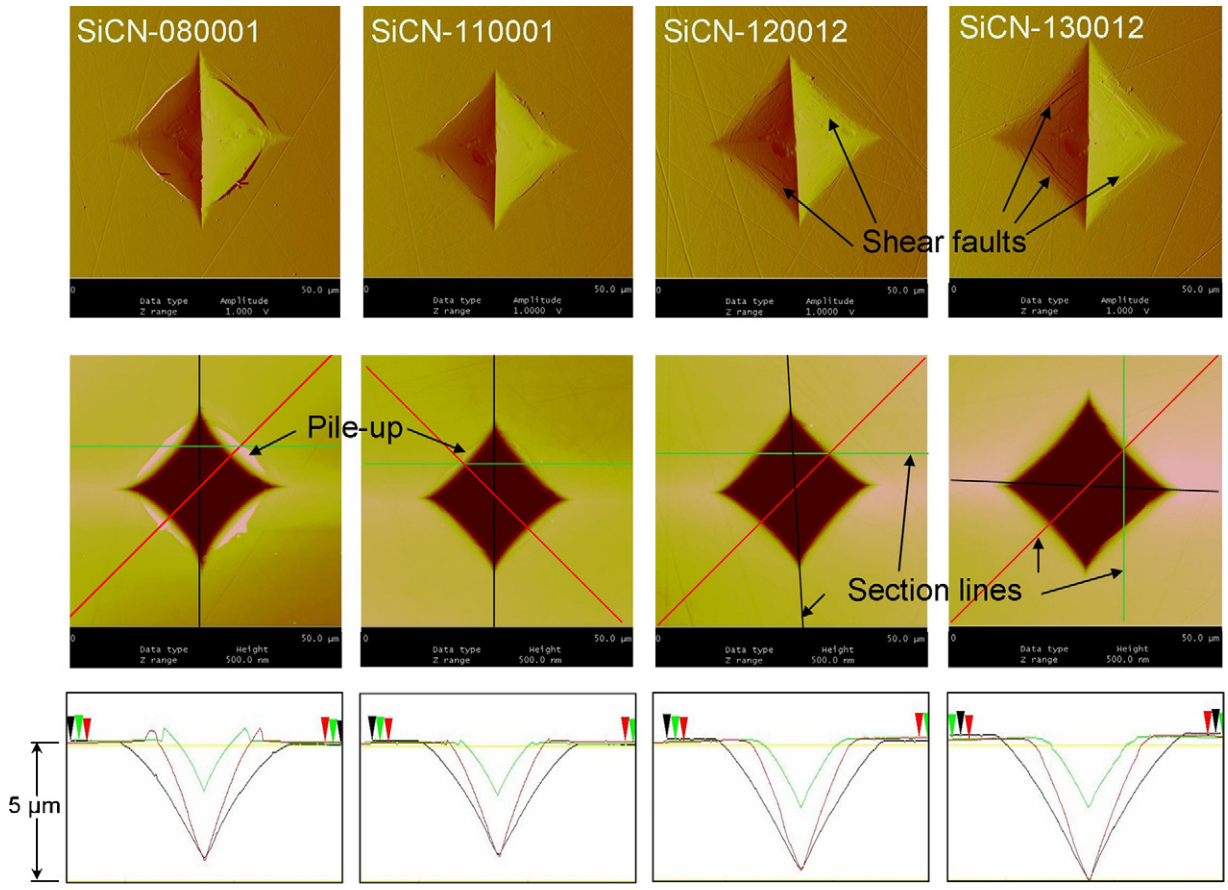

Fig. 9. Tapping mode AFM topographic images of Vickers micro-indents obtained at $P = 4.905$ N in SiCN-080001, SiCN-110001, SiCN-120012 and SiCN-130012 showing features of plastic deformation. Illustrations in the first, second and third rows are from amplitude contrast imaging, height contrast imaging and sectional analysis of height contrast images respectively. Width of the images = 50 μm.

4. Discussion

A first hand comparison of the determined elastic moduli and hardness from the present nanoindentation analysis shows that the quantities are in agreement with the range of E and H values reported for precursor-derived Si–C–O (50 GPa $\leq E \leq$ 130 GPa; 4 GPa $\leq H \leq$ 9 GPa),[3] Si–C ($H \approx 12$ GPa),[5] Si–C–N ($E \approx 120$ GPa, $H \approx 13$ GPa)[16] and a-CN_x:H materials (110 GPa $\leq E \leq$ 170 GPa; 6 GPa $\leq H \leq$ 12 GPa),[29,30] determined from various experimental techniques. The evolution of E and H also correlate well with the structural evolution across the range of investigated materials. As mentioned in Section 2, the latter was effected by changing the degree of polymer-to-ceramic transformation by progressively increasing the final pyrolysis temperature from 800 to 1300 °C. Accordingly, while the materials SiCN-080001 through SiCN-100001 possess an electron-amorphous structure, progressively increasing network connectivity in the amorphous structure is realized due to the progressive stripping of one-fold coordinated hydrogen from the initial Si–C–N–H network in these materials.[20] This transformation leads to an increase in the network density and rigidity[31] and thereby, an increased resistance to deformation manifested in the E and H values. The effect of dehydrogenation in improving the mechanical properties of tetrahedrally coordinated amorphous carbon has been well documented,[29,30] and has also been reported with respect to precursor-derived Si–C–O ceramics.[3] With the further increase in pyrolysis temperature above 1100 °C, a progressive phase separation and organization of turbostratic graphite (TG) is realized in the present Si–C–N ceramics, the materials SiCN-120012 and SiCN-130012 falling in this category.[20] Due to the lower density and deformation resistance intrinsic to the TG phase, combined with a weakening effect in disrupting the continuous Si–C–N tetrahedral network, the latter materials display a progressive drop in the mechanical properties, again reflected in the presently determined E and H values. The effect of the precipitation of sp^2 graphitic carbon within a sp^3 tetrahedral carbon network in lowering the mechanical properties has also been shown in the literature.[30,32] The material SiCN-110001 – although being electron-amorphous[20] – lies in the borderline between the electron-amorphous and phase-separated material categories, which is responsible for the peculiar inflexions in its mechanical behavior observed in Sections 3.1–3.5. In fact, nucleation and organization of sp^2-hybridized carbon is observed in the present materials pyrolyzed at 800 °C upwards.[20] Thus, it is clear that the influence of the graphitic phase becomes effective only above a critical size of its organization within the Si–C–N matrix, which is presumably just reached in the material SiCN-110001.

The elastic moduli derived from nanoindentation show significant deviations from the mean elastic moduli of the whole specimens determined from the resonance frequency testing. However, as the moduli determined independently from spherical and Berkovich indentation analyses agree well with each other, it can be reasoned that the elastic properties of the material volume probed by the nanoindentation measurements are truly determined and representative of the local material behavior. The observed deviation of the local properties from the bulk elastic behavior can originate from (i) a gradient in structure, composition or residual stresses across the specimen cross-section, or (ii) the inherent difference in the material response to the two experimental techniques. The observation of the above deviations in different directions for amorphous and phase-separated materials additionally suggests that the evolution of either the gradients or the material response showed an inflexion. Development of structural and stress gradients can be expected from the special nature of the PDC synthesis, where a differential precursor-to-ceramic transformation across the material bulk inevitably occurs due to the constraints imposed by the sample dimensions on the pyrolytic effluents and transformation induced shrinkage.[3,20] Evaluation of the nature and magnitude of these gradients is an involving task in itself and offers scope for future investigation. However, since the individual deviations are limited to ~10% spread over the entire specimen bulk, and as the nanoindentation measurements offer the advantage of probing the local mechanical properties ($h_{max} \ll 0.01w$, w = specimen thickness), the present efforts are restricted to the understanding of the properties from the local material behavior.

From the analysis of P–h load–unload cycle, it is found that the elastic and plastic deformations in amorphous materials SiCN-080001 through SiCN-100001 evolve in a fixed proportion, approximately equal to that in fused silica. This proportion, quantified in terms of the plastic work ratio (W_{pl}/W_{tot}) displays an approximately constant value of 0.34 for all the above four materials. This value represents one of the lowest among the experimentally recorded plastic work ratios for fully developed plastic contacts, and signifies the high elastic recovery observed in these materials. Along with the anomalous densification behavior,[11,27,33] the high elastic recovery in fused silica is well documented.[19,21,34] On the other hand, the anomalous character of materials SiCN-080001 through SiCN-110001 has been recently confirmed from the typical indentation crack patterns and the evaluated low residual contact stresses.[15] Thus, it seems that a low plastic work ratio is characteristic of materials that undergo pronounced densification under the indenter. In other words, the elastic *as well as* plastic deformation in these materials can be understood as a volume deformation-controlled process.

A significant increase in the hardness of the amorphous materials SiCN-080001 through SiCN-100001 is also found at increasing indentation load, while the plastic work ratio remains constant at the above low value, even when the residual depth ratio increases. Notably, a similar invariance of the plastic work ratio at increasing residual depth ratio has been reported for fused silica (Fig. 7 in Ref. 34). Recently, Perriot et al. showed using diamond anvil cell (DAC) experiments, Raman microspectroscopy and FE calculations that indentation induced densification in fused silica leads to strain hardening.[35] Thus, it is evident that the observed indentation deformation behavior of materials SiCN-080001 through SiCN-100001 and fused silica has implications on ISE and strain hardening, and is related to their densifying type of plastic deformation. In materials capable of densification, the enhancement of plastic deformation at increasing applied loads (or ISE, tending to lower hardness) and the concomitant evolution of strain hardening compete with each other in determining the material resistance to deformation. This can explain the near invariance of hardness of fused silica and the small but significant increase of nanoindentation hardness in the above amorphous Si–C–N materials. Yoshida et al. experimentally evaluated the relative fractions of densification and shear flow during nanoindentation of silicate glasses including fused silica, where a decrease in the fraction of densification was observed at increasing loads.[33] Noting that fused silica strain-hardens during densification, it is understandable that a progressive plastic deformation by densification at increasing loads will also simultaneously reduce the capability of the deformed material for further densification. At saturation density this deformed material will be expected to behave in a 'normal' manner, i.e., deform further by shear flow. This is indeed observed at the core of the indentations in the case of materials SiCN-080001 and SiCN-110001, evident in Fig. 9.

While strain hardening explains the evolution of hardness in the amorphous materials SiCN-080001 through SiCN-100001, the decrease of hardness at higher loads in the phase-separated materials SiCN-120012 and SiCN-130012 reveals that the enhanced plastic deformation at higher loads leading to ISE dominates over the strain hardening effect, due to the emergence of additional plastic deformation mechanisms. A microstructural examination shows that the latter is effected by the shear deformation of the graphitic phase in these materials. A similar influence of the graphitic precipitation on the strain hardening characteristics of glass-like carbons was reported by Iwashita et al.[32] Thus, in contrast to the amorphous Si–C–N materials, the plastic deformation in phase-separated materials is predominantly an interface deformation-controlled process. However, the persistence of densification deformation in promoting strain hardening in these materials is revealed in the microindentation analysis, in spite of the effect of the graphitic precipitation. Evidently, this contribution arises from the amorphous Si–C–N matrix phase.

5. Conclusions

The elastic and plastic deformation behavior of precursor-derived Si–C–N ceramics was investigated using depth-sensing nanoindentation. The elastic moduli and nanoindentation hardness evaluated from the analysis of the load–displacement curves correlated well with the evolution of material resistance to elastic and plastic deformation, commensurate with the structural and microstructural evolution in the materials. Analysis of the work of indentation during the load–unload cycle highlighted the characteristics of anomalous plastic deformation in the electron-amorphous Si–C–N materials. The contrasting evolution of

elastic and plastic deformation work quantities in amorphous and phase-separated materials indicate that the plastic deformation in former materials was volume deformation-controlled whereas that in the latter materials was interface deformation-controlled. The consequence of the densifying type of plastic deformation in promoting strain hardening behavior in these materials was identified from the load dependant increase in hardness, to a measurable extent in the nanoindentation load regime and to an appreciable extent in the microindentation load regime. The capacity of the phase-separated materials for strain hardening was relatively lower than the amorphous materials. The pile-up and sink-in behavior was in agreement with the strain hardening capability of the materials.

Acknowledgements

The financial support for this work was provided by the *Max-Planck-Gesellschaft*.

References

1. Bill, J. and Aldinger, F., Precursor-derived covalent ceramics. *Adv. Mater.*, 1995, **7**, 775–787.
2. Monthioux, M. and Delverdier, O., Thermal behavior of (organosilicon) polymer-derived ceramics. 5. Main facts and trends. *J. Eur. Ceram. Soc.*, 1996, **16**, 721–737.
3. Walter, S., Soraru, G. D., Brequel, H. and Enzo, S., Microstructural and mechanical characterization of sol gel-derived Si–O–C glasses. *J. Eur. Ceram. Soc.*, 2002, **22**, 2389–2400.
4. Bauer, A., PhD thesis, University of Stuttgart, 2002.
5. Moraes, K. V. and Interrante, L. V., Processing, fracture toughness, and Vickers hardness of allylhydridopolycarbosilane-derived silicon carbide. *J. Am. Ceram. Soc.*, 2003, **86**, 342–346.
6. Janakiraman, N., Burghard, Z. and Aldinger, F., Fracture toughness evaluation of precursor-derived Si–C–N ceramics using the crack opening displacement approach. *J. Non-Cryst. Solids*, 2009, **355**, 2102–2113.
7. Célarié, F., Prades, S., Bonamy, D., Ferrero, L., Bouchaud, E., Guillot, C. *et al.*, Glass breaks like metal, but at the nanometer scale. *Phys. Rev. Lett.*, 2003, **90**, 075504.
8. Guin, J. P. and Wiederhorn, S. M., Fracture of silicate glasses: ductile or brittle? *Phys. Rev. Lett.*, 2004, **92**, 215502.
9. Janakiraman, N. and Aldinger, F., Fracture in precursor-derived Si–C–N ceramics—analysis of crack roughness and damage mechanisms. *J. Non-Cryst. Solids*, 2009, **355**, 2114–2121.
10. Marsh, D. M., Plastic flow in glass. *Proc. R. Soc. Lond. Ser. A*, 1964, **279**, 420–435.
11. Neely, J. E. and Mackenzie, J. D., Hardness and low-temperature deformation of silica glass. *J. Mater. Sci.*, 1968, **3**, 603–609.
12. Klaffke, D., Wasche, R., Janakiraman, N. and Aldinger, F., Tribological characterisation of siliconcarbonitride ceramics derived from preceramic polymers. *Wear*, 2006, **260**, 711–719.
13. Liew, L., Zhang, W., Bright, V. M., An, L., Dunn, M. L. and Raj, R., Fabrication of SiCN ceramic MEMS using injectable polymer-precursor technique. *Sens. Actuators*, 2001, **89**, 64–70.
14. Rouxel, T., Sanglebœuf, J.-C., Guin, J.-P., Keryvin, V. and Soraru, G. D., Surface damage resistance of gel-derived oxycarbide glasses: hardness, toughness, and scratchability. *J. Am. Ceram. Soc.*, 2001, **84**, 2220–2224.
15. Burghard, Z., PhD thesis, University of Stuttgart, 2004.
16. Galusek, D., Riley, F. L. and Riedel, R., Nanoindentation of a polymer-derived amorphous silicon carbonitride ceramic. *J. Am. Ceram. Soc.*, 2001, **84**, 1164–1166.
17. Soraru, G. D., Dallapiccola, E. and D'Andrea, G., Mechanical characterization of sol–gel-derived silicon oxycarbide glasses. *J. Am. Ceram. Soc.*, 1996, **79**, 2074–2080.
18. Shah, S. R. and Raj, R., Mechanical properties of a fully dense polymer derived ceramic made by a novel pressure casting process. *Acta Mater.*, 2002, **50**, 4093–4103.
19. Oliver, W. C. and Pharr, G. M., An improved technique for determining hardness and elastic-modulus using load and displacement sensing indentation experiments. *J. Mater. Res.*, 1992, **7**, 1564–1583.
20. Janakiraman, N. and Aldinger, F., Fabrication and characterization of fully dense Si–C–N ceramics from a poly(ureamethylvinyl)silazane precursor. *J. Eur. Ceram. Soc.*, 2009, **29**, 163–173.
21. Cheng, Y. T. and Cheng, C. M., Scaling, dimensional analysis and indentation measurements. *Mater. Sci. Eng. R*, 2004, **44**, 91–149.
22. Cheng, Y. T. and Cheng, C. M., Further analysis of indentation loading curves: effects of tip rounding on mechanical property measurements. *J. Mater. Res.*, 1998, **13**, 1059–1064.
23. Oliver, W. C. and Pharr, G. M., Measurement of hardness and elastic modulus by instrumented indentation: advances in understanding and refinements to methodology. *J. Mater. Res.*, 2004, **19**, 3–20.
24. Moysan, C., Riedel, R., Harshe, R., Rouxel, T. and Augereau, F., Mechanical characterization of a polysiloxane-derived SiOC glass. *J. Eur. Ceram. Soc.*, 2007, **27**, 397–403.
25. Herbert, E. G., Pharr, G. M., Oliver, W. C., Lucas, B. N. and Hay, J. L., On the measurement of stress–strain curves by spherical indentation. *Thin Solid Films*, 2001, **398–399**, 331–335.
26. Attaf, M. T., New ceramics related investigation of the indentation energy concept. *Mater. Lett.*, 2003, **57**, 4684–4693.
27. Arora, A., Marshall, D. B. and Lawn, B. R., Indentation deformation-fracture of normal and anomalous glasses. *J. Non-Cryst. Solids*, 1979, **31**, 415–428.
28. Qian, L. M., Li, M., Zhou, Z., Yang, H. and Shi, X., Comparison of nano-indentation hardness to microhardness. *Surf. Coat. Technol.*, 2005, **195**, 264–271.
29. Tanaka, D., Ohshio, S. and Saitoh, H., Nano-indentation for structural analysis of hydrogen- and nitrogen-containing carbon films. *Jpn. J. Appl. Phys.*, 2000, **39**, 6008–6015.
30. Ohkawara, Y., Ohshio, S., Suzuki, T., Ito, H., Yatsui, K. and Saitoh, H., Quantitative analysis of hydrogen in amorphous films of hydrogenated carbon nitride. *Jpn. J. Appl. Phys.*, 2001, **40**, 7007–7012.
31. Boolchand, P., Zhang, M. and Goodman, B., Influence of one-fold-coordinated atoms on mechanical properties of covalent networks. *Phys. Rev. B*, 1996, **53**, 11488–11494.
32. Iwashita, N., Swain, M. V., Field, J. S., Ohta, N. and Bitoh, S., Elasto-plastic deformation of glass-like carbons heat-treated at different temperatures. *Carbon*, 2001, **39**, 1525–1532.
33. Yoshida, S., Sanglebœuf, J.-C. and Rouxel, T., Quantitative evaluation of indentation-induced densification in glass. *J. Mater. Res.*, 2005, **20**, 3404–3412.
34. Tan, M., A study of indentation work in homogeneous materials. *J. Mater. Res.*, 2006, **21**, 1363–1374.
35. Perriot, A., Vandembroucq, D., Barthel, E., Martinez, V., Grosvalet, L., Martinet, C. *et al.*, Raman microspectroscopic characterization of amorphous silica plastic behavior. *J. Am. Ceram. Soc.*, 2006, **89**, 596–601.